nature chemical biology

ARTICLES

https://doi.org/10.1038/s41589-020-0510-4

Drug antagonism and single-agent dominance result from differences in death kinetics

Ryan Richards[1], Hannah R. Schwartz[1], Megan E. Honeywell[1], Mariah S. Stewart[1], Peter Cruz-Gordillo[1], Anna J. Joyce[1], Benjamin D. Landry[1] and Michael J. Lee[1,2,3]✉

Cancer treatment generally involves drugs used in combinations. Most previous work has focused on identifying and understanding synergistic drug–drug interactions; however, understanding antagonistic interactions remains an important and understudied issue. To enrich for antagonism and reveal common features of these combinations, we screened all pairwise combinations of drugs characterized as activators of regulated cell death. This network is strongly enriched for antagonism, particularly a form of antagonism that we call 'single-agent dominance'. Single-agent dominance refers to antagonisms in which a two-drug combination phenocopies one of the two agents. Dominance results from differences in cell death onset time, with dominant drugs acting earlier than their suppressed counterparts. We explored mechanisms by which parthanatotic agents dominate apoptotic agents, finding that dominance in this scenario is caused by mutually exclusive and conflicting use of Poly(ADP-ribose) polymerase 1 (PARP1). Taken together, our study reveals death kinetics as a predictive feature of antagonism, due to inhibitory crosstalk between cell death pathways.

Cancer therapies are often limited by acquired drug resistance and partial killing of a tumor cell population[1,2]. To combat these limitations, many efforts focus on the development of combination drug therapies[3–5]. Generally, previous studies have focused on identifying combinations that produce synergistic drug–drug interactions. In contrast to expectations, recent reports demonstrate that synergy is not observed in clinically efficacious drug combinations, in which the drugs instead are typically additive or act independently[6]. Synergistic combinations tend to reinforce the killing that would be induced by one of the drugs within the combination, rather than facilitating the killing of new cells that would not be killed by either of the drugs alone[7,8]. Furthermore, synergistic combinations favor the evolution of resistant clones[9]. While these data may limit the value of identifying drug synergies, understanding the sources of antagonism still remains an important issue. It stands to reason that antagonism—particularly very strong response antagonism—may limit the efficacy of a drug combination. Predicting which drug combinations will result in antagonism is challenging due to the lack of transparent 'rules' underlying this phenomenon and the unpredictable and often genotype-specific nature of drug–drug interactions[10]. Thus, an unmet need is the identification of robust guiding principles to more efficiently identify, predict or improve antagonistic drug–drug interactions.

In the absence of principles that enable prediction of non-additive drug interactions, a common approach is to screen drug combinations, prioritizing testing for drugs that target proteins with complementary functions. Recent studies have used known or predicted network topologies to enrich for non-additive drug combinations[11–14]. Furthermore, network simulations have revealed topological features, such as negative feedback and mutual inhibition, which may underlie the antagonism of drug combinations[15]. We envisioned that the principles of drug–drug antagonism might emerge from studying drugs targeting a network enriched for antagonistic interactions.

In recent years, it has become clear that at least 12 mechanistically distinct forms of cell death exist[16]. Because these death pathways function in a mutually exclusive manner, we reasoned that drug combinations designed to co-activate multiple types of cell death might be enriched for antagonistic interactions. Several lines of evidence exist to suggest negative interaction and/or interdependent and mutually exclusive function among the various forms of cell death[17,18]. For instance, necroptosis requires inhibition of extrinsic apoptosis due to cleavage of the pro-necroptotic receptor-interacting protein kinase 1 (RIPK1) by caspase-8 (ref. [19]). Similarly, PARP1, the initiator of parthanatos, is cleaved by caspase-3, suggesting that apoptosis inhibits the ability to activate parthanatos[20]. From these data, a model is beginning to emerge that mutually exclusive activation of cell death pathways may be enforced through inhibitory 'crosstalk' between death regulatory pathways[16].

To identify a robust set of antagonistic interactions, we tested all pairwise combinations of the canonical activators for different cell death subtypes. We find that drug combinations consisting of cell death-targeting drugs are enriched for drug antagonism and, in particular, are strongly enriched for an extreme form of antagonism that we call single-agent dominance (SAD). In SAD, the two-drug combination phenocopies one of the two single drugs. Importantly, this occurs even when the dominant drug is the less efficacious of the two compounds. Using statistical modeling, we find that a key feature driving SAD is a discrepancy in the relative timing of cell death onset, with faster-acting drugs suppressing slower-acting drugs, leading to strong antagonism. These antagonistic phenotypes could be relieved by temporally phasing drug addition to promote synchronized co-activation of multiple death pathways. Finally, we explore the molecular mechanisms of SAD involving apoptotic and parthanatotic agents, finding that mutually exclusive but conflicting use of PARP1 drives dominance in these scenarios. Taken together, these findings highlight that the interconnected nature of cell death causes unexpected behaviors when these pathways are co-activated.

[1]Program in Systems Biology (PSB), University of Massachusetts Medical School, Worcester, MA, USA. [2]Program in Molecular Medicine (PMM), University of Massachusetts Medical School, Worcester, MA, USA. [3]Department of Molecular, Cell and Cancer Biology (MCCB), University of Massachusetts Medical School, Worcester, MA, USA. ✉e-mail: michael.lee@umassmed.edu

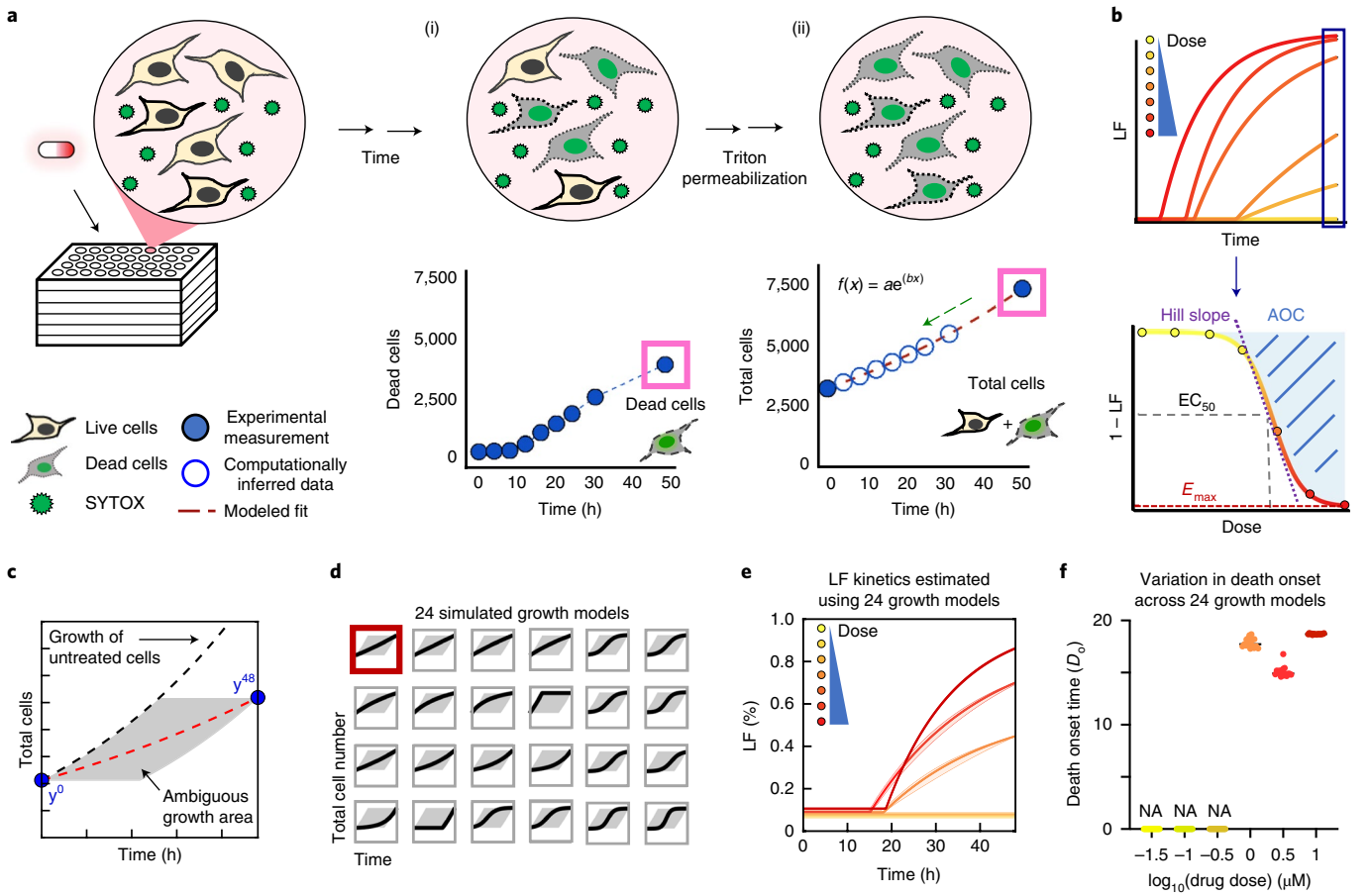

Fig. 1 | A high-throughput assay to monitor cell death kinetics. a, Schematic of the SYTOX assay. (i) Dead cells are counted over time using SYTOX fluorescence. (ii) After permeabilization, total cell counts can be determined at 0-h and 48-h time points (filled blue circles). Total cell counts at intermediate times are inferred by modeling to an exponential fit (red dashed line). **b**, Modeled total cell counts used to infer LF at all time points. LF is fit to a kinetic model to quantify death onset (D_O) and rate (D_R) following cell permeabilization. Percentage viability at 48 h is used to quantify pharmacological parameters. See also Supplementary Figs. 1 and 2. **c–f**, Death kinetic estimates under varied population growth models. **c**, Ambiguity of growth over time of a drug-treated population. Experimental measurements for total cells were made only at the beginning (y_0) and end (y_{48}) of the assay. Any trajectory through the gray area is feasible. The red dashed line is the exponential model used in this study. The black dashed line is the growth rate of untreated cells. Example data shown are from cells treated with 0.1 μM camptothecin. **d**, Twenty-four varied growth models evaluated. The red box highlights the exponential growth model. Other growth models tested included linear and sigmoidal models and models with non-uniform rates over time. **e**, LF kinetics for camptothecin at various doses, computed using the different estimated growth models shown in **d**. The thick line is the exponential model. The shaded area around the line represents s.d. among the 24 simulated growth models in **d**. See also Supplementary Dataset 1. **f**, Range of death onset times computed for different doses of camptothecin. Each dot is the D_O estimated using a different population growth model from **d**. N/A, not applicable.

Furthermore, death onset time is a feature of antagonistic drug responses, with a previously unappreciated role in dictating interactions between cell death processes.

Results

A high-throughput assay for monitoring death kinetics. Drugs that induce different forms of death vary substantially in terms of their efficacy and activation rate[21]. To evaluate drug combinations consisting of apoptotic and non-apoptotic agents, we first developed an assay that could be performed in high throughput while also retaining accurate analysis of death kinetics. Methods have been developed for high-throughput measurement of cell death using SYTOX green in a fluorescence plate reader[17]. Furthermore, SYTOX fluorescence is specific to cell death but largely agnostic to the mechanism by which cells die[22]. We made experimental and computational modifications to previous methods to enable an accurate inference of the numbers of live, dead and total cells (Fig. 1a and Supplementary Fig. 1). Understanding drug-induced death kinetics requires quantification of both live and dead cells over time, as inferences built from either measurement alone can be misleading (Supplementary Fig. 1b)[21]. To gain these insights, we measured the lethal fraction (LF; the percentage of dead cells relative to total cells) before drug addition and at the end of the assay (Fig. 1a). To determine LF at intermediate times, experimentally measured dead cell numbers were compared to computationally inferred total cell numbers at matching time points (Fig. 1a,b). We estimated total cell numbers using an exponential model, constrained by the observed population size at the beginning and end of the assay. Although the growth of drug-treated cells is not likely to always be exponential and may not even be uniform over time, simulations of LF kinetics under varied population growth models revealed similar values regardless of which growth model was chosen (Fig. 1c–f and Supplementary Fig. 1). This procedure enables quantification of drug-induced changes in growth rate, death rate and LF over time, including an analytical estimation of death onset time (Fig. 1b). Furthermore, all measurements are computed from a single assay, without the need for any specialized equipment.

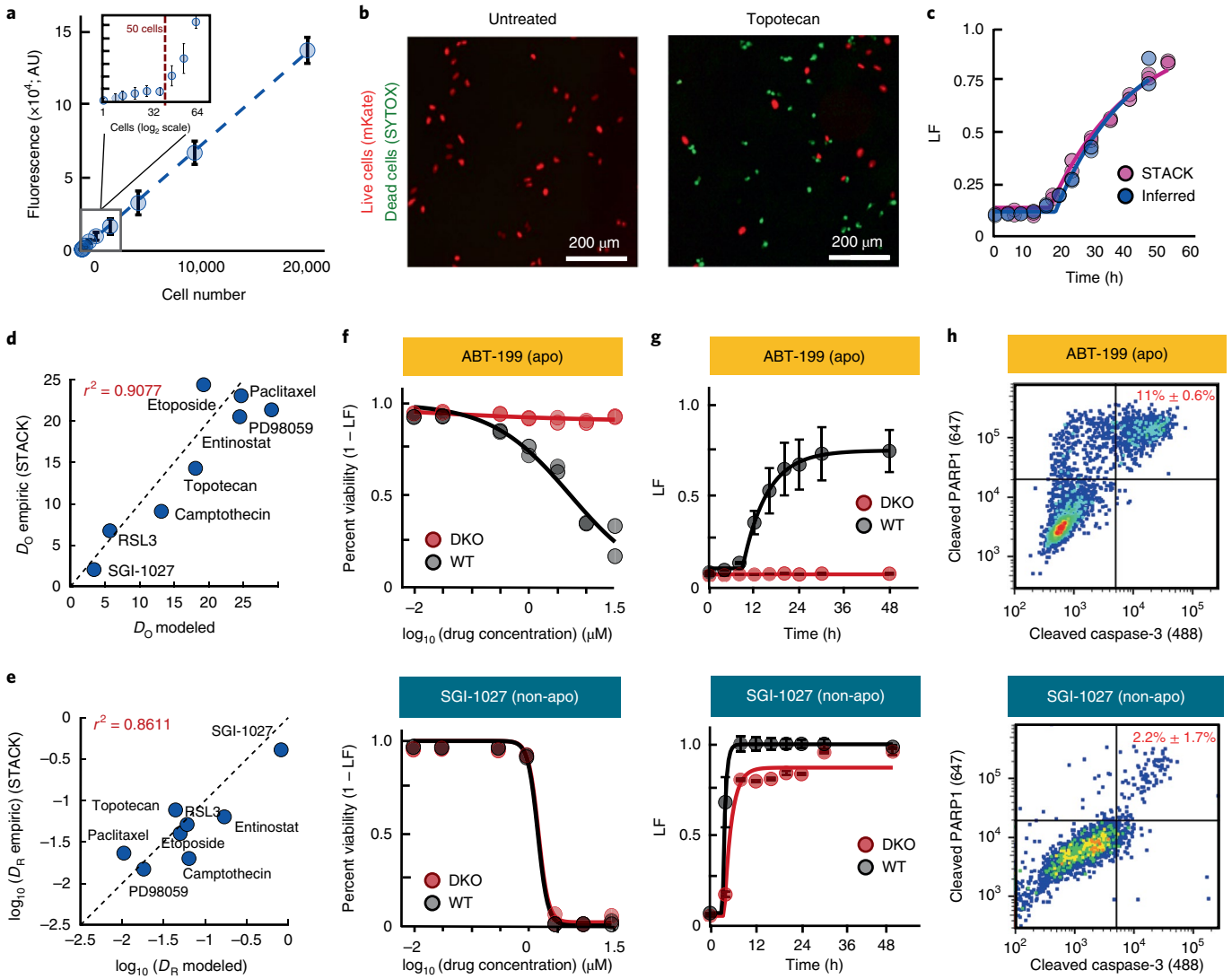

Fig. 2 | Accurate analysis of death kinetics for apoptotic and non-apoptotic agents. a, SYTOX plate reader sensitivity. AU, arbitrary units. **b**–**e**, Computational estimates of death kinetics compared to experimental measurements using STACK[21]. Data are the mean ± s.d. from biological replicates ($n = 6$). **b**, Example images from cells treated with topotecan (31.6 μM) or left untreated. Images are representative of four independent experiments, each with similar results. **c**–**e**, Comparisons between plate reader-based estimates and STACK for LF data and kinetic fits for topotecan as in b (**c**) and death onset time (**d**) and death rate (**e**) for drugs with varied mechanisms of action. For **d** and **e**, each drug was tested at a saturating LF_{max} dose (3.16–31.6 μM). **f**–**h**, Examples of apoptotic (top) and non-apoptotic (bottom) drugs. Drugs were tested in WT or DKO U2OS cells at seven doses over 48 h. See also Supplementary Fig. 3–5. **f**, Percentage viability across doses at 48 h. **g**, LF kinetics at the highest drug concentration. Data are the mean ± s.d. from biological replicates ($n = 4$). **h**, Apoptosis quantified by flow cytometry. Cleaved PARP1 and cleaved caspase-3 double positivity was quantified 24 h after treatment. Percentages are the mean ± s.d. from biological replicates ($n = 3$).

Kinetic analysis for apoptotic and non-apoptotic agents. To evaluate assay sensitivity, we tested cell dilutions over a wide range of cell concentrations. SYTOX green fluorescence of U2OS cells was linearly correlated with cell number from approximately 50–20,000 cells per well, allowing accurate quantification of death rates even as low as 1% above background (Fig. 2a). To determine the accuracy of our assay, and in particular the accuracy of our death rate estimates, we compared our approach to STACK, an automated microscopy-based approach that enables direct measurement of live and dead cells[21]. Overall, we found a strong correlation between our computationally inferred death rates and those computed from direct measurement of live and dead cells (Fig. 2b–e and Supplementary Fig. 2).

To determine whether our assay could reliably measure death induced by both apoptotic and non-apoptotic mechanisms, we quantified responses to a panel of 54 drugs reported to kill cells using different forms of regulated cell death[16,23–30]. Drug responses were screened in U2OS cells, a cancer cell line with wild-type (WT) p53, which respond well to a diverse array of cell death-inducing agents. Because of the limited availability of markers for some forms of death, we focused on a simplified classification scheme, categorizing drugs as non-lethal, apoptotic or non-apoptotic. Non-lethal compounds were those whose effects were exclusively due to modulation of growth rate without any drug-induced killing (Supplementary Fig. 3a,b). To distinguish between apoptotic and non-apoptotic drugs, we scored the degree to which the observed response was modulated in a *BAX* and *BAK* double-knockout (DKO) genetic background, relative to WT U2OS cells (Fig. 2f–h and Supplementary Fig. 3). *BAX* and *BAK* are pro-apoptotic members of the BCL-2 family and are pore-forming proteins required

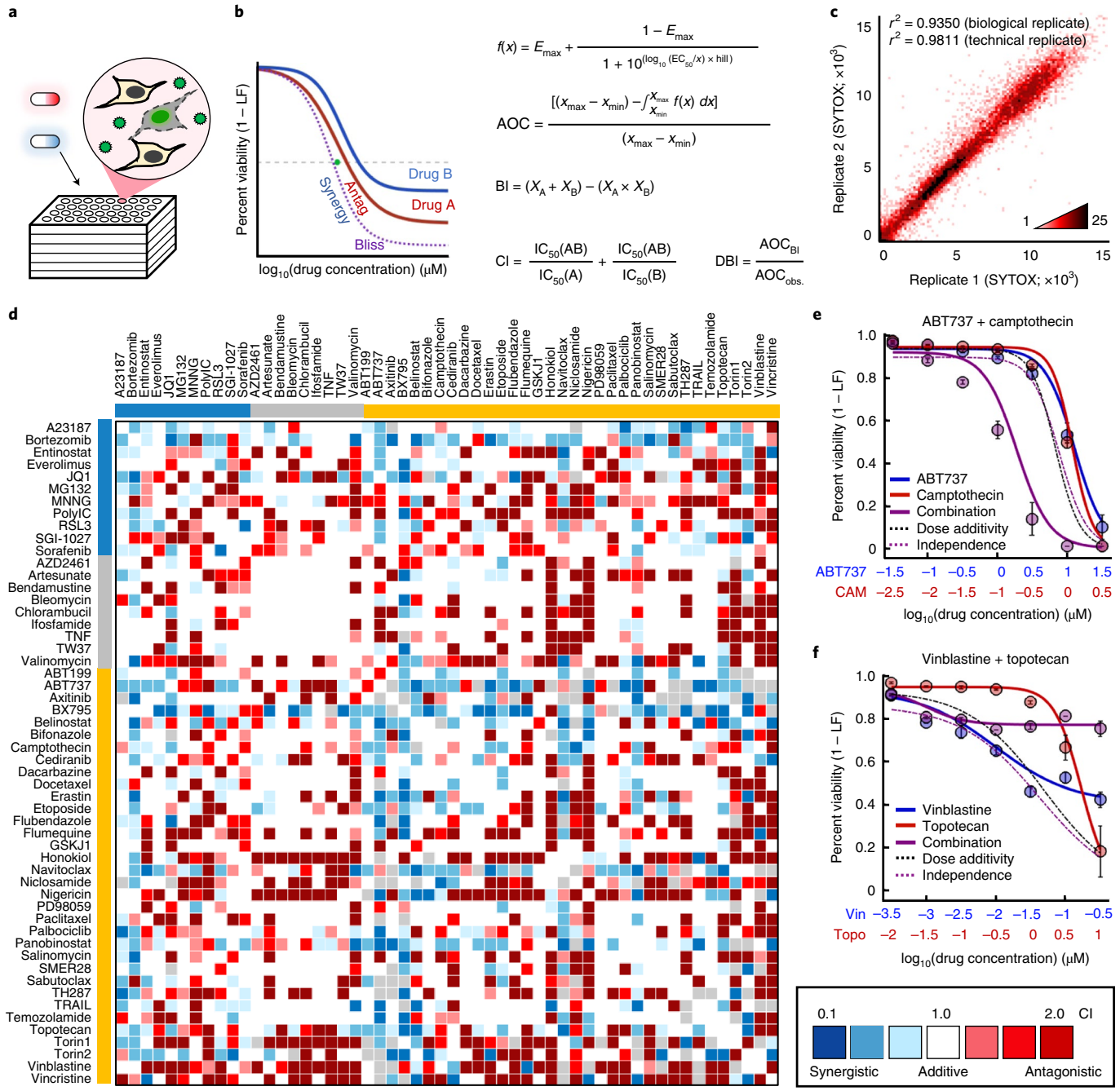

Fig. 3 | Combination drug screen to evaluate co-activation of apoptotic and non-apoptotic death pathways. a, SYTOX assay for drug combinations. **b**, Calculation of drug–drug interactions. Equations are shown for calculating dose curves, expectation under Bliss independence (BI), combination index (CI; green dot) and deviation from Bliss independence (DBI). **c,** Density plot of replicates from the drug combination screen. The Pearson correlation coefficient is shown for biological replicates (tested across different days; $n = 2$) and technical replicates (tested across multiple wells of a plate; $n = 2$). **d**, Drug combination screen. Heat map of all CIs determined from screening 54 × 54 drug combinations. Colored bars depict drug class: blue, non-apoptotic; gray, non-lethal; gold, apoptotic. See also Supplementary Figs. 6 and 7. **e**,**f**, Examples of synergistic and antagonistic drug combinations. **e**, ABT737 (blue) and camptothecin (red). **f**, Vinblastine (blue) and topotecan (red). For **e** and **f**, purple corresponds to observed combinations; dashed black lines are the prediction assuming dose additivity; and dashed purple lines are the prediction assuming drug independence. Data are the mean ± s.d. from biological replicates ($n = 4$).

for mitochondrial outer membrane permeabilization[31]. We defined drugs that primarily induce apoptosis as those in which the maximum LF was decreased by greater than 50% in DKO as compared to WT cells (Supplementary Figs. 3–5). Of the 54 drugs profiled, 34 were apoptotic using this threshold. Eleven drugs primarily induced non-apoptotic death, as drug sensitivity was largely unchanged in DKO cells (Fig. 2f–h and Supplementary Fig. 3). To validate the use of a 50% threshold, we also used multivariate analyses such as principal-component analysis (PCA) and *t*-distributed stochastic neighbor embedding (*t*-SNE), which integrated the kinetic and pharmacological data for each drug and did not require thresholds for the degree of difference between WT and DKO cells (Supplementary Fig. 3f,g). Both PCA and *t*-SNE recovered the same classifications as our simplified maximum LF (LF_{max})-based

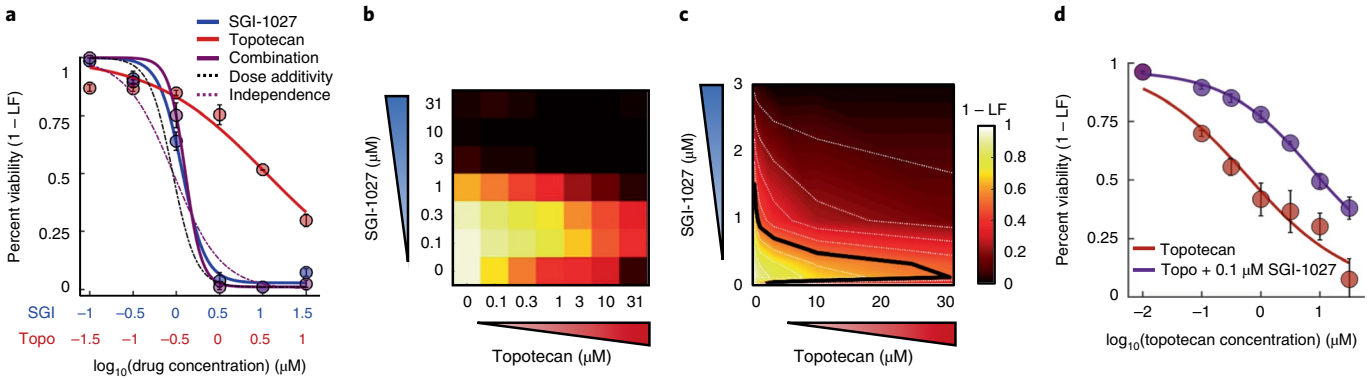

Fig. 4 | Combinations of apoptotic and non-apoptotic cell death drugs are enriched for antagonism and single-agent dominance. a, Example SAD combination. Drugs were given at a constant dose ratio, and cell death was measured using SYTOX at 48 h. Blue, SGI-1027; red, topotecan; purple, combination; the dashed black line shows the expection given dose additivity,and the dashed purple line shows the expection given response independence. **b**, Percentage viability response matrix for all-by-all dose combinations. **c**, Isobologram analysis of **b**. Doses are plotted on a linear scale with 10% isobols shown and 50% isobols highlighted with a black line. **d**, Values of 1−LF for topotecan alone at varied doses (red) or topotecan in the presence of 0.1 μM SGI-1027. Data are the mean ± s.d. from independent biological replicates ($n = 4$).

convention. Drug classifications based on relative DKO versus WT sensitivity also agreed with categorization based on caspase-3 cleavage, a marker of apoptosis (Fig. 2h). Thus, our computational inference-based method accurately quantifies drug-induced death and death kinetics for a wide variety of drugs, including those with apoptotic and non-apoptotic mechanisms.

Co-activation of death pathways causes antagonism. Different subtypes of cell death are activated in a mutually exclusive manner due to inhibitory interactions between death pathways[16]. These features are common among antagonistic interactions[15]. We next tested whether co-activation of multiple death pathways would enrich for drug antagonism. Our strategy was to test all pairwise combinations of the 54 cell death-activating drugs that we evaluated as single agents. All combinations were tested across seven doses at a fixed dose ratio (constant-ratio dosing) and responses were measured at nine time points over 48 h (Fig. 3a,b). Drugs were tested on multiple days and across wells on a given day, and both technical and biological replicates were highly correlated, suggesting a high degree of reproducibility within our assay (Fig. 3c and Supplementary Fig. 6).

To score drug–drug interactions, we focused on two common reference models for estimating the expected response in the absence of interactions: the Chou–Talalay combination index (CI) and the deviation from Bliss Independence (DBI). CI calculates interactions by comparing the observed half-maximal inhibitory concentration (IC_{50}) for a drug combination to that expected assuming dose additivity, whereas DBI calculates interactions by comparing the observed response to that expected given independent action for the two single drugs (Fig. 3d and Supplementary Fig. 7a,b)[32–34]. Both reference models are supported by well-validated quantitative principles; however, as CI is focused on dose additivity and DBI is calculated relative to response independence, these models tend to capture different types of interactions[35–37]. For both models, thresholds for synergy and antagonism were determined by identifying CI or DBI values that produced less than 5% false-positive rates when comparing experimental replicates (Supplementary Fig. 7). Drug–drug interaction scores were highly reproducible on retesting with other assays (Fig. 3e,f and Supplementary Fig. 6).

In our combinatorial drug screen, approximately half of all combinations resulted in a drug–drug interaction (53.4% by CI; 46.6% by DBI). Furthermore, regardless of the scoring convention used, greater than 30% of all combinations resulted in antagonism (Supplementary Table 1). By comparison, other large-scale screens consisting of 'random' combinations have identified antagonism at frequencies of 2–10% (Supplementary Fig. 8)[11,38–40]. Thus, as expected, combinations of cell death-activating drugs are strongly enriched for antagonistic drug–drug interactions.

Death-inducing drug pairs yield single-agent dominance. To more deeply analyze our data, we focused on a large set of strong antagonisms that we uncovered (Supplementary Fig. 8a). We noticed that many antagonistic responses were of an unexpected form, wherein the two-drug combination phenocopied one of the two single agents (Fig. 4a), which we call SAD. The characteristic feature of SAD is that an otherwise efficacious drug becomes fully suppressed by a second agent. For example, both SGI-1027, a DNA methyltransferase 1 (DNMT1) inhibitor that induces non-apoptotic death, and topotecan, a topoisomerase I inhibitor that induces apoptosis, produced strong killing in U2OS cells when applied as single agents (Fig. 4a). The combination of these agents, however, resulted in precisely the same response as SGI-1027 alone. One trivial explanation for this phenotype could be that highly potent drugs tend to dominate simply because no additional cells remain to be killed. To test this idea directly, we examined all dose–dose combinations to determine whether low concentrations of a dominant drug could suppress high concentrations of a suppressed drug. We found that even non-efficacious concentrations of SGI-1027 were sufficient to block death induced by high concentrations of topotecan (Fig. 4b–d).

To identify other drug combinations that feature SAD, we quantified the Euclidean distance in dose-response profiles between every drug combination and its two component drugs. We focused only on combinations that were antagonistic and required that a suppressed drug induce significant levels of death when used alone. Overall, we identified 130 SAD combinations, which were 30% of all antagonistic interactions (Supplementary Fig. 9).

Death onset time is a key determinant of drug dominance. Considering the prominence of the SAD phenotype in our data, we sought to deepen our understanding of dominant antagonism by identifying features that were enriched within SAD combinations. We performed a multivariate analysis on the kinetic and pharmacological data generated in our screen. PCA was used to reduce dimensionality. Six principal components were identified that captured over 85% of the variation in drug-induced death kinetics and pharmacological measurements (Fig. 5a–c). To determine which

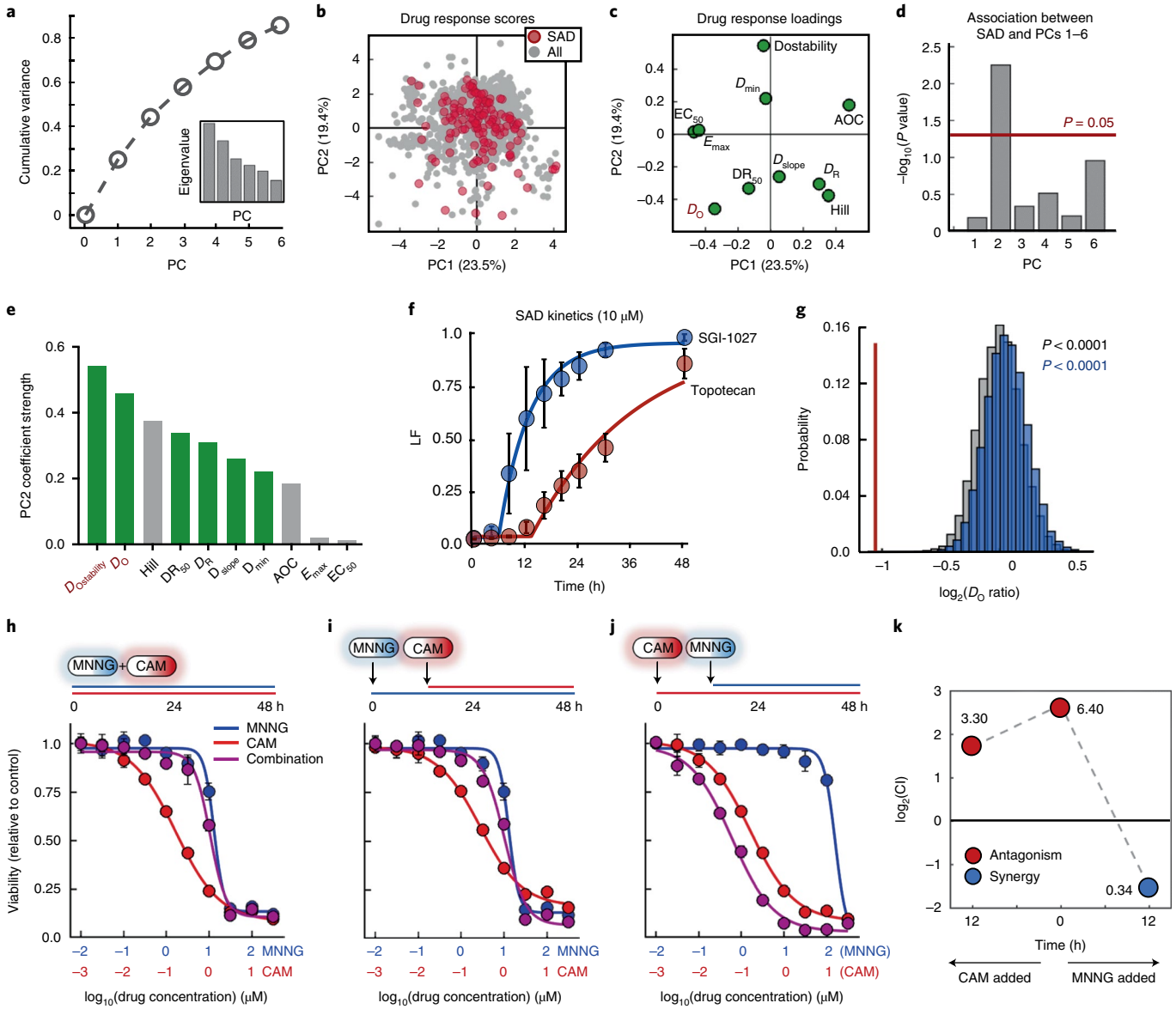

Fig. 5 | Statistical modeling reveals death onset kinetics as a key determinant of SAD combinations. a, Cumulative variation captured by PCs 1–6. Inset, eigenvalues for PCs 1–6. **b**, PCA scores plot for all single drugs and combinations from the cell death screen. Red, SAD combinations; gray, other combinations. **c**, Loadings plot for PCs 1 and 2. **d**, Enrichment of SAD for PCs 1–6. Enrichment for each PC was calculated using a one-tailed Fisher's exact test. For **b**–**d**, data are from the drug combination screen shown in Fig. 3 (54 single drugs; 1,431 combinations; $n = 4$ biological replicates). **e**, Absolute value of parameter loading coefficients on PC2. Green, rate metrics; gray, pharmacological metrics. **f**, LF kinetics for an example SAD combination. Blue, dominant drug; red, suppressed drug. **g**, Distribution of average onset ratios for all combinations (gray), non-SAD combinations (blue) and SAD combinations (red). Empiric *P* values were calculated by bootstrapping 10,000 iterations of 130 random drug combinations. **h**–**j**, Dose–response functions for MNNG and camptothecin combinations when drugs were added simultaneously (**h**) or sequentially (**i**,**j**). Blue, MNNG; red, camptothecin; purple, combination. **k**, CI values over time for MNNG + camptothecin. Red, antagonism; blue, synergism. For **f** and **h**–**j**, data are the mean ± s.d. from biological replicates ($n = 4$).

dimensions were capturing information related to drug dominance, we scored the statistical enrichment for SAD combinations on each PC. SAD combinations were enriched only on PC2, which captured 19% of the overall drug response variation (Fig. 5d and Supplementary Fig. 10).

Considering the enrichment for SAD combinations on PC2, we next identified the drug response features captured uniquely on this component. The response loading coefficients revealed that features related to cell death onset time (D_O and $D_{Ostability}$) were the variables most strongly associated with SAD combinations (Fig. 5c,e). D_O refers to the estimated death onset time from our kinetic measurements, while $D_{Ostability}$ refers to the similarity of onset times for a given drug across doses. Features that are related to potency, such as the area over the curve (AOC), E_{max} (maximum efficiency) and half-maximal effective concentration (EC_{50}), were not captured on this component. To determine what aspect of death onset time was related to dominance, we examined death kinetics for the individual drugs that made up SAD combinations. We noticed a discrepancy in the activation rates for dominant and suppressed drugs. For instance, in combinations

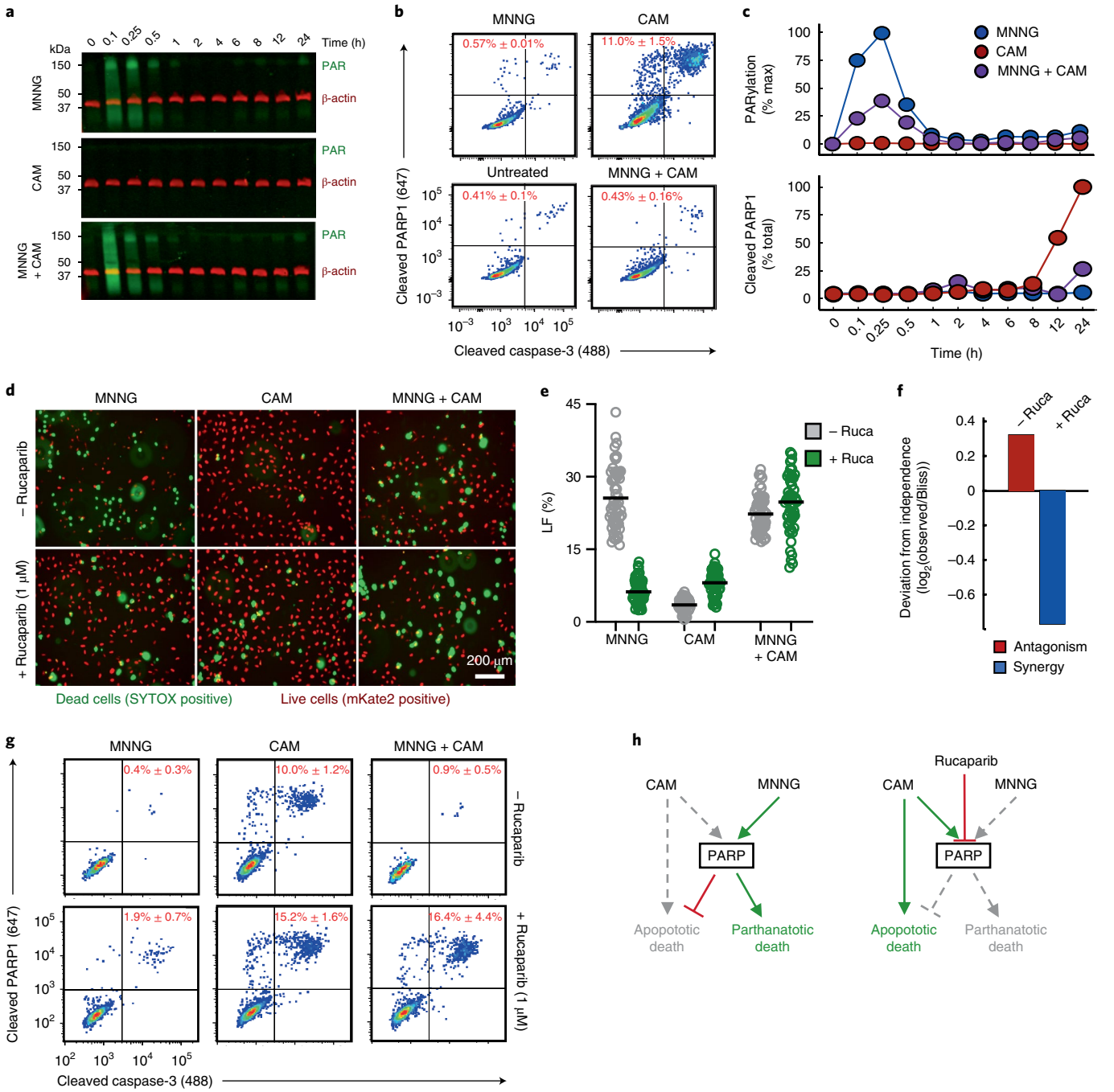

Fig. 6 | PARP1-dependent interactions mediate single-agent dominance and choice between parthanatotic and apoptotic death. a–c, Dynamics of drug-induced changes in PARP1 activity. Samples were treated with MNNG (31.6 μM), camptothecin (3.16 μM) or MNNG + camptothecin for the indicated times. **a**, Representative western blot of total protein PARylation. Green, total PAR; red, β-actin. Data are representative of two biological replicates. See also Supplementary Fig. 13a. **b**, Cleaved PARP1 quantified by fluorescence-activated cell sorting (FACS; 12-h treatment). Data are the percentage of cleaved PARP1 shown as the mean ± s.d. from independent biological replicates ($n = 2$). **c**, Quantification of PAR (top) and cleaved PARP1 (bottom) activation dynamics. PAR is quantified as the percentage of the maximum signal. Cleaved PARP1 is shown as the percentage of total cells. Data are the mean from independent biological replicates ($n = 2$). **d**, Live-cell imaging using STACK. U2OS cells expressing nuclear-localized mKate2 (red) were treated with MNNG, camptothecin or MNNG + camptothecin, with or without 1 μM rucaparib. Representative images are shown from 48 h after treatment from two independent replicates. **e**, Quantification of the imaging in **d**. Data are the LF per image (50 images per condition). The line represents the mean per treatment condition. **f**, Deviation from the expected response. The expected combination response was calculated relative to BI using the quantified LF values from **e**. **g**, Apoptotic activity of MNNG + camptothecin. Cleaved PARP1 and cleaved caspase-3 were quantified 12 h after treatment. Data are the mean ± s.d. from independent biological replicates ($n = 4$). **h**, A model for a PARP-mediated interaction between parthanatotic and apoptotic death leading to SAD.

of SGI-1027 and topotecan, in which SGI-1027 was dominant, SGI-1027 killed cells earlier and at a faster rate than topotecan (Fig. 5f). To determine whether differences in activation rates were a common feature of SAD combinations, we explored the kinetic ratios for all 130 SAD combinations compared to those from 10,000 iterations of 130 random drug combinations in our

data. This analysis confirmed that dominant drugs activate significantly earlier than their suppressed counterparts (Fig. 5g).

To test whether the correlation between onset time asymmetry and drug dominance was indicative of a causal relationship, our strategy was to temporally stagger the addition of dominant drugs, such that their activity occurred concomitantly with that of their suppressed counterparts. We tested this concept with the combination of *N*-methyl-*N*′-nitro-*N*-nitrosoguanidine (MNNG) and camptothecin, which results in robust domination by MNNG (Fig. 5h). Addition of the suppressed drug later in time relative to the dominant drug did not affect overall drug response or the degree of MNNG dominance (Fig. 5i); however, antagonism and dominance were relieved when MNNG addition was staggered such that the suppressed agent was active at the same time as the dominant drug (Fig. 5j,k).

To further test the robustness of the association between dominance and onset time asymmetry, we tested the extent to which drug dominance for a given combination would be conserved in other cell contexts. In our preliminary drug titrations for this study, we found several drugs for which rates differed significantly across cell lines. For instance, ABT199 induced death faster in MDA-MB-231 cells, whereas panobinostat induced death much later in A549 cells as compared to other cells. Alternatively, SGI-1027 tended to activate death rapidly across all cell lines tested. To determine whether these rate differences altered drug dominance or if SAD combinations would persist even in the absence of onset time asymmetry, we retested SAD combinations in other cell lines. Combinations of SGI-1027 and camptothecin consistently produced dominance in other cell lines (Supplementary Fig. 11a–c). Thus, when onset time asymmetry was observed in other cell lines, drug dominance was conserved. Alternatively, when death onset times differed in other cell contexts, drug dominance also changed. Combinations of ABT737 and ABT199 ceased to produce dominance in MDA-MB-231 cells, where the onset times for these drugs were similar (Supplementary Fig. 11d–f). BX795 and panobinostat, which induced death with similar onset times in U2OS cells, produced a SAD phenotype in A549 cells, a context in which panobinostat killed with similar efficacy but was activated later than in U2OS cells (Supplementary Fig. 11g–i). Thus, these data suggest that faster-acting drugs suppress slower-acting drugs, leading to antagonism and SAD.

Predictive modeling to identify new SAD combinations. To further determine the generalizability of our findings, we aimed to predict new SAD combinations from drugs that have not yet been tested in combination. Although onset time asymmetry was a characteristic of SAD combinations, our data suggest that this feature alone would poorly predict dominance. To identify other important features for generating drug dominance, we explored our PCA map to determine additional characteristics of SAD combinations, dominant drugs or the relationships between dominant and suppressed drugs. Our PCA analysis showed that SAD combinations were enriched only on PC2; however, when comparing dominant and suppressed drugs rather than their combinations, we found that dominant drugs were significantly farther away from their suppressed counterparts, suggesting that the vector projections of single drugs could themselves be used to predict new SAD combinations (Supplementary Fig. 12a–c).

We mined publicly available data for pharmacological and kinetic response profiles for single drugs, which could be projected into our PCA map. From these single-drug projections, we identified drug pairs whose projection was similar to that observed for experimentally identified SAD combinations (Supplementary Fig. 12d). Full kinetic data for drugs at varied doses were not available; however, data were available for limited doses for a large panel of drugs from a recent study that explored cell death kinetics[21]. We incorporated these kinetic data with publicly available pharmacological data for drug responses in U2OS cells[41], and together these data were used to determine probable vector projections for new drugs in PC1 and PC2 (Supplementary Fig. 12d).

Using this publicly available data, we tested 77 combinations among 15 drugs, including 48 combinations whose relative single-agent profiles suggested drug dominance. We validated these predictions using our SYTOX-based death assay (Supplementary Fig. 12e–g). Our validation screen was strongly enriched for antagonism (>60%), and 77% of the predicted SAD combinations resulted in a dominant antagonistic interaction ($P = 2.3 \times 10^{-5}$; Supplementary Fig. 12h,i). Thus, even in the absence of information about the drugs and their mechanisms of action, an analysis of single-drug death kinetic properties was sufficient to identify new SAD combinations.

Interactions between death pathways mediate dominance. Our drug combination screen and subsequent computational analyses revealed the overall prevalence and a critical mechanism driving drug dominance. Next, we sought to gain a molecular understanding of these drug–drug interactions. Non-additivity is a feature often related to the underlying network structure of a drug's target proteins[12]. Given the diversity of drugs tested and the limited understanding of death regulatory pathways, we studied a SAD combination featuring drugs with known regulatory pathway interactions. For example, hyperactivation of PARP1 causes parthanatos, a form of non-apoptotic death[16,42]. Conversely, inhibition of PARP1 causes apoptosis due to 'PARP trapping' and stabilization of DNA lesions[43]. Furthermore, PARP1 is cleaved and inactivated by caspase-3 (ref. [20]). These data suggest a negative interaction between apoptotic and parthanatotic pathways, possibly due to the conflicting use of PARP1. To test this, we first evaluated the pathway activation dynamics of parthanatotic and apoptotic drugs at the level of PARP1 activation/inhibition. MNNG exposure led to transient hyperactivation of PARP1, causing increased protein PARylation (Fig. 6a). PARP1 hyperactivation began minutes after drug exposure and returned to baseline in 1 h. When cells were treated with apoptotic drugs like camptothecin, PARP1 was not activated but rather was cleaved and inactivated by caspase-3 (Fig. 6b) approximately 8–12 h after camptothecin exposure (Fig. 6c). Thus, following exposure to MNNG or camptothecin, perturbations to PARP1 activity occur in distinct temporal windows and in a mutually exclusive manner. When cells were exposed to both MNNG and camptothecin, PARP1 activation followed an MNNG-like dynamic pattern, consistent with the observed phenotypic dominance by MNNG over camptothecin (Fig. 6a–c).

Having determined that parthanatotic and apoptotic perturbations of PARP1 occur in a mutually exclusive manner, we next examined whether PARP1 is mechanistically involved in the MNNG–camptothecin SAD phenotype. To do so, we explored the fate of cells treated with MNNG and/or camptothecin in the presence or absence of a PARP1 inhibitor, rucaparib. Although PARP1 inhibition by rucaparib can induce apoptosis, a sublethal dose was sufficient for blocking PARP1 activity (Supplementary Fig. 13). Consistent with expectations, PARP1 inhibition blocked MNNG-mediated death but enhanced camptothecin sensitivity (Fig. 6d,e). The dominance of MNNG over camptothecin was lost when PARP1 was inhibited by rucaparib. Instead, in the presence of rucaparib, combinations of MNNG and camptothecin led to synergistic levels of cell death (Fig. 6f). Parthanatotic death, by definition, should not occur when PARP1 is inhibited[16]. Thus, we suspected that PARP1 inhibition changed not only the nature of the drug–drug interaction but also the mechanism of death induced by this combination. To test this, we evaluated markers of activation of apoptotic cell death. Using flow cytometry to measure caspase-3 activation, we found that PARP1 inhibition by rucaparib switched the mechanism of killing induced by MNNG–camptothecin combinations from parthanatotic to apoptotic cell death (Fig. 6g,h). Thus, these data

confirm that PARP1 mediates an interaction between parthanatotic and apoptotic death pathways, leading to antagonism and SAD.

Discussion

When defining drug–drug interactions, a common goal is to identify drug combinations that may be beneficial therapies. For many years, an implicit assumption was that drug synergy was conceptually interchangeable with clinical benefit; however, recent studies have challenged that previous thinking[6–8]. Drug synergy, at least when defined relative to a dose-additivity reference, generally suggests that similar results could be obtained at a lower dose. Synergy does not guarantee that a combination will kill cells that would not have been killed by either agent alone. Similarly, antagonism may not be clinically harmful, even for some SAD combinations. For instance, a simple explanation for some SAD combinations would be that both drugs have the capacity to kill the same population of cells. These combinations would score as antagonistic relative to a response-independence reference (but additive relative to dose additivity). In this study, however, we found that combinations consisting of death-activating drugs tend to induce antagonism when compared to both dose-additivity and response-independence references (Supplementary Fig. 7). Furthermore, the maximum response of many SAD combinations involved killing of fewer cells than were killed by at least one of the two component drugs. In these cases, it is likely that using these drugs in combination rather than individually would negatively affect treatment efficacy.

Importantly, our study reveals some promising avenues for ways to generate potent combinations of death-inducing drugs. In the case of MNNG and camptothecin, these drugs alone and in combination can kill to the same fractional limit, leaving ~10% viable cells at saturating doses. Interestingly, when these drugs were temporally phased to relieve MNNG dominance, the overall killing increased to 98%, suggesting that correctly timed drug combinations could kill cells that would not have been killed by drug A or B alone.

The phenotypes uncovered in this study underscore the complexities of death regulation and the need for a greater mechanistic understanding of how different forms of cell death are controlled, with regard to both the molecular mechanisms and kinetics of activation. Regulated cell death provides an attractive target for therapeutic intervention, as cell killing is required for curative therapies[44]. Many different mechanisms are likely contributing to the SAD combinations identified in this study, including modulation of cell cycle progression (in particular, when cell cycle inhibitors are combined with drugs that are more toxic to cells in S phase). As we demonstrated in the case of parthanatos and apoptosis, however, pathway crosstalk likely accounts for many non-additive responses observed in these drug combinations. This case is particularly important, as PARP1 inhibitors are being tested in clinical settings, generally in combination with other cytotoxic therapies, and without regard to whether these companion therapies induce apoptotic or parthanatotic death[45,46]. Thus, for PARP inhibitors, our data suggest that the effectiveness of these agents should depend on the mechanisms by which companion compounds kill cells and, more importantly, the relative rates of activation of these drugs. More generally, considering the overall degree of antagonism and SAD within combinations of cell death-targeting drugs, our data highlight the potential existence of widespread inhibitory crosstalk between death pathways. In most cases, however, we simply lack requisite knowledge of the death pathways activated by each drug and the molecular mechanisms by which most forms of cell death are regulated.

A major benefit from our study is the identification of a generalizable principle that can be used to streamline the evaluation of drug combinations, namely that rates of drug-induced cell death can be used to predict drug antagonisms[6]. Because drug–drug interactions are difficult to predict, current strategies rely on screening drug combinations. This process is laborious due to the combinatorial expansion of possible combinations to test, which is further complicated by the fact that drug–drug interactions often depend on the doses used, the order and environment in which the drugs are applied, and the genotype(s) under evaluation[5,10,47–49]. Our study suggests that drugs may not need to be tested in combination to avoid SAD combinations if the rates of drug-induced death onset are known or can be measured (Supplementary Fig. 14). Furthermore, our data suggest that rate asymmetry may be a more reliable predictor of SAD than the identity of the drugs themselves. Using rates, we correctly predicted new SAD combinations among drugs that had not been previously tested. Also, we found that drug pairs that produced SAD phenotypes often differed across cell lines; however, these cell-type-specific differences could also be predicted on the basis of death onset asymmetry. These data suggest an opportunity for a new paradigm in cancer therapy, one that prioritizes conserved rules rather than conserved drug identities.

Currently, standard approaches do not typically evaluate drug activation kinetics, instead focusing on the relationship between efficacy/potency and dose. These 'dose–response' relationships have been the central focus of drug pharmacology data for over a century, and they clearly reveal important insights about a given drug. The kinetic features of a drug are generally not predictable from single-time-point dose–response data. Our study reveals that these 'rate-response' relationships are observable in kinetic data and that they also produce unique insights into the nature of a given drug or drug combination. Given the complementarity of pharmacological and kinetic data, the evaluation of both types of data should become a new standard.

Online content

Any Nature Research reporting summaries, source data, extended data, supplementary information, acknowledgements, peer review information; details of author contributions and competing interests; and statements of data and code availability are available at https://doi.org/10.1038/s41589-020-0510-4.

Received: 15 October 2019; Accepted: 28 February 2020;
Published online: 06 April 2020

References

1. Al-Lazikani, B., Banerji, U. & Workman, P. Combinatorial drug therapy for cancer in the post-genomic era. *Nat. Biotechnol.* **30**, 1–13 (2012).
2. Roux, J. et al. Fractional killing arises from cell-to-cell variability in overcoming a caspase activity threshold. *Mol. Syst. Biol.* **11**, 803–817 (2015).
3. Kummar, S. et al. Utilizing targeted cancer therapeutic agents in combination: novel approaches and urgent requirements. *Nat. Rev. Drug Discov.* **9**, 843–856 (2010).
4. Pemovska, T., Bigenzahn, J. W. & Superti-Furga, G. ScienceDirect Recent advances in combinatorial drug screening and synergy scoring. *Curr. Opin. Pharmacology* **42**, 102–110 (2018).
5. Lee, M. J. et al. Sequential application of anticancer drugs enhances cell death by rewiring apoptotic signaling networks. *Cell* **149**, 780–794 (2012).
6. Palmer, A. C. & Sorger, P. K. Combination cancer therapy can confer benefit via patient-to-patient variability without drug additivity or synergy. *Cell* **171**, 1678–1682 (2017).
7. Pritchard, J. R. et al. Defining principles of combination drug mechanisms of action. *Proc. Natl Acad. Sci. USA* **110**, E170–E179 (2013).
8. Zhao, B., Pritchard, J., Lauffenburger, D. & Hemann, M. Addressing genetic tumor heterogeneity through computationally predictive combination therapy. *Cancer Discov.* **4**, 166–174 (2014).
9. Michel, J.-B., Yeh, P. J., Chait, R., Moellering, R. C. & Kishony, R. Drug interactions modulate the potential for evolution of resistance. *Proc. Natl Acad. Sci. USA* **105**, 14918–14923 (2008).
10. Koplev, S. et al. Dynamic rearrangement of cell states detected by systematic screening of sequential anticancer treatments. *Cell Rep.* **20**, 2784–2791 (2017).
11. Miller, M. et al. Drug synergy screen and network modeling in dedifferentiated liposarcoma identifies CDK4 and IGF1R as synergistic drug targets. *Sci. Signal.* **6**, ra85 (2013).
12. Jaeger, S. et al. Quantification of pathway cross-talk reveals novel synergistic drug combinations for breast cancer. *Cancer Res.* **77**, 459–469 (2017).
13. Cokol, M. et al. Systematic exploration of synergistic drug pairs. *Mol. Syst. Biol.* **7**, 1–9 (2011).

14. Simpkins, S. W. et al. Predicting bioprocess targets of chemical compounds through integration of chemical–genetic and genetic interactions. *PLoS Comput. Biol.* **14**, e1006532–31 (2018).
15. Yin, N. et al. Synergistic and antagonistic drug combinations depend on network topology. *PLoS ONE* **9**, e93960–e93967 (2014).
16. Galluzzi, L. et al. Molecular mechanisms of cell death: recommendations of the Nomenclature Committee on Cell Death 2018. *Cell Death Differ.* **25**, 1–56 (2018).
17. Grootjans, S. et al. A real-time fluorometric method for the simultaneous detection of cell death type and rate. *Nat. Protoc.* **11**, 1444–1454 (2016).
18. Hitomi, J. et al. Identification of a molecular signaling network that regulates a cellular necrotic cell death pathway. *Cell* **135**, 1311–1323 (2008).
19. Newton, K. et al. Cleavage of RIPK1 by caspase-8 is crucial for limiting apoptosis and necroptosis. *Nature* **574**, 1–18 (2019).
20. Soldani, C. & Scovassi, A. Poly(ADP-ribose) polymerase-1 cleavage during apoptosis: an update. *Apoptosis* **7**, 321–328 (2002).
21. Forcina, G. C., Conlon, M., Wells, A., Cao, J. & Dixon, S. J. Systematic quantification of population cell death kinetics in mammalian cells. *Cell Syst.* **4**, 1–18 (2017).
22. Wlodkowic, D., Faley, S., Darzynkiewicz, Z. & Cooper, J. M. Real-time cytotoxicity assays. *Methods Mol. Biol.* **731**, 285–291 (2011).
23. Louandre, C. et al. Iron-dependent cell death of hepatocellular carcinoma cells exposed to sorafenib. *Int. J. Cancer* **133**, 1732–1742 (2013).
24. Chiu, L.-Y., Ho, F.-M., Shiah, S.-G., Chang, Y. & Lin, W.-W. Oxidative stress initiates DNA damager MNNG-induced poly(ADP-ribose) polymerase-1-dependent parthanatos cell death. *Biochem. Pharmacol.* **81**, 459–470 (2011).
25. Eling, N., Reuter, L., Hazin, J., Hamacher-Brady, A. & Brady, N. R. Identification of artesunate as a specific activator of ferroptosis in pancreatic cancer cells. *Oncoscience* **2**, 517–532 (2015).
26. Berghe, T., Linkermann, A., Jouan-Lanhouet, S., Walczak, H. & Vandenabeele, P. Regulated necrosis: the expanding network of non-apoptotic cell death pathways. *Nat. Rev. Mol. Cell Biol.* **15**, 135–147 (2014).
27. Jouan-Lanhouet, S. et al. TRAIL induces necroptosis involving RIPK1/RIPK3-dependent PARP-1 activation. *Cell Death Differ.* **19**, 1–12 (2019).
28. Dixon, S. J. et al. Ferroptosis: an iron-dependent form of nonapoptotic cell death. *Cell* **149**, 1060–1072 (2012).
29. Axelrod, M. et al. Combinatorial drug screening identifies compensatory pathway interactions and adaptive resistance mechanisms. *Oncotarget* **4**, 622–635 (2013).
30. Laster, S., Wood, J. & Gooding, L. Tumor necrosis factor can induce both apoptotic and necrotic forms of cell lysis. *J. Immunol.* **141**, 2629–2634 (1988).
31. Wei, M. et al. Proapoptotic BAX and BAK: a requisite gateway to mitochondrial dysfunction and death. *Science* **292**, 727–730 (2001).
32. Russ, D. & Kishony, R. Additivity of inhibitory effects in multidrug combinations. *Nat. Microbiol.* **3**, 1–9 (2018).
33. Chou, T.-C. & Talalay, P. Quantitative analysis of dose–effect relationships: the combined effects of multiple drugs or enzyme inhibitors. *Adv. Enzym. Regul.* **22**, 27–55 (1984).
34. Tallarida, R. J. The interaction index: a measure of drug synergism. *Pain* **98**, 163–168 (2002).
35. Chou, T.-C. Drug combination studies and their synergy quantification using the Chou–Talalay method. *Cancer Res.* **70**, 440–446 (2010).
36. Baeder, D. Y., Yu, G., Hozé, N., Rolff, J. & Regoes, R. R. Antimicrobial combinations: Bliss independence and Loewe additivity derived from mechanistic multi-hit models. *Philos. Trans. R. Soc. B Biol. Sci.* **371**, 20150294-11 (2016).
37. Lederer, S., Dijkstra, T. M. & Heskes, T. Additive dose response models: explicit formulation and the Loewe additivity consistency condition. *Front. Pharmacol.* **9**, 31 (2018).
38. O'Neil, J. et al. An unbiased oncology compound screen to identify novel combination strategies. *Mol. Cancer Ther.* **15**, 1155–1162 (2016).
39. Holbeck, S. L. et al. The National Cancer Institute ALMANAC: a comprehensive screening resource for the detection of anticancer drug pairs with enhanced therapeutic activity. *Cancer Res.* **77**, 3564–3576 (2017).
40. Menden, M. P. et al. Community assessment to advance computational prediction of cancer drug combinations in a pharmacogenomic screen. *Nat. Commun.* **10**, 1–17 (2019).
41. Rees, M. G. et al. Correlating chemical sensitivity and basal gene expression reveals mechanism of action. *Nat. Chem. Biol.* **12**, 109–116 (2016).
42. Wang, Y. et al. A nuclease that mediates cell death induced by DNA damage and poly(ADP-ribose) polymerase-1. *Science* **354**, aad6872 (2016).
43. Zimmermann, M. et al. CRISPR screens identify genomic ribonucleotides as a source of PARP-trapping lesions. *Nature* **559**, 285–289 (2018).
44. Merino, D. et al. BH3-mimetic drugs: blazing the trail for new cancer medicines. *Cancer Cell* **34**, 879–891 (2018).
45. Farmer, H. et al. Targeting the DNA repair defect in *BRCA* mutant cells as a therapeutic strategy. *Nature* **434**, 917–921 (2005).
46. Yap, T. A., Plummer, R., Azad, N. S. & Helleday, T. In *American Society of Clinical Oncology Educational Book* 185–195 (2019)
47. Landry, B. D. et al. Tumor–stroma interactions differentially alter drug sensitivity based on the origin of stromal cells. *Mol. Syst. Biol.* **14**, e8322-15 (2018).
48. Marusyk, A. et al. Spatial proximity to fibroblasts impacts molecular features and therapeutic sensitivity of breast cancer cells influencing clinical outcomes. *Cancer Res.* **76**, 6495–6506 (2016).
49. Lehmann, B. D. et al. Identification of human triple-negative breast cancer subtypes and preclinical models for selection of targeted therapies. *J. Clin. Invest.* **121**, 1–18 (2011).

Methods

Cell lines and reagents. U2OS, A549, MCF10A and MDA-MB-231 cells were obtained from the American Type Culture Collection (ATCC) and maintained at low passage numbers (generally less than 20 passages from the original vial). U2OS, A549 and MDA-MB-231 cells were grown in DMEM supplemented with 10% FBS, 2 mM glutamine and penicillin-streptomycin. MCF10A cells were grown in DMEM/F12 medium supplemented with 5% horse serum, 20 ng ml^{-1} epidermal growth factor (EGF), 0.5 mg ml^{-1} hydrocortisone, 100 ng ml^{-1} cholera toxin, 10 µg ml^{-1} insulin and penicillin-streptomycin. Drugs were purchased from Selleck Chemicals, APEXBio Technology or Sigma-Aldrich. SYTOX green was purchased from Thermo Fisher. Anti-poly/mono ADP ribose rabbit monoclonal antibody (83732) was purchased from Cell Signaling Technology. Purified rabbit anti-active caspase-3 (559565) and Alexa Fluor 647-conjugated mouse anti-cleaved PARP (558710) antibodies were purchased from BD Pharmingen. Secondary antibodies were purchased from LICOR Biosciences and BD Biosciences. See also Supplementary Table 2.

SYTOX-based measurement of cell death. The total number of dead cells at given time points can be determined by measuring SYTOX fluorescence. SYTOX green was tested for linearity by plating cells at twofold cell dilutions from 20,000 cells to one cell in 5 µM SYTOX. After adhering, cells were lysed with 0.1% Triton in PBS for 1.5 h. Fluorescence was measured on a Tecan M1000 plate reader with excitation at 503 nm and emission at 524 nm. Gain was set to capture linearity and for fluorescence to be at ~85% saturation of the detector. For drug-induced cell death measurements, cells were seeded at 1,500 cells per well of 384-well optical-bottom black-walled plates or 2,500 cells per well of 96-well optical-bottom black-walled plates and adhered overnight on the day before drug addition ('day −1'). On day 0, drugs were prepared at a 5× final concentration (10× for 96-well experiments) in DMEM containing 25 µM SYTOX green (50 µM in 96-well experiments). Seven-point half-log dilutions were prepared in 96-well plates. Drug dilutions were added using an Integra ViaFlo96 electronic pipettor (Integra). Fluorescence readings (excitation at 504 nm, emission at 523 nm) were taken at 0, 4, 8, 12, 16, 20, 24, 30 and 48 h on a Tecan M1000 plate reader. Additionally, an untreated plate was lysed at $t=0$ for initial cell counts by adding 0.1% Triton in PBS and incubating for 1.5 h at 37 °C with 5% CO_2. After the 48-h reading, all experimental wells were lysed and a final fluorescence reading was taken. LF and relative viability were calculated using the fluorescence readings before and after Triton permeabilization.

Modeling lethal fraction kinetics. Using the procedure above, an LF measurement can be experimentally determined only at 0 and 48 h (Supplementary Fig. 1a). To determine LF at intermediate time points, it was necessary to estimate the growth of the drug-treated cells from 0 to 48 h, as the number of dead cells can in some cases produce false insights (for example, for drugs that induce potent cell death very quickly at high doses and more slowly at low doses, lower doses can yield more dead cells; Supplementary Fig. 1b). Although the population size at the beginning (y_0) and end (y_{48}) of the assay is experimentally determined, some ambiguity exists regarding the shape/kinetics of population growth in the drug-treated conditions (that is, the dynamics of population growth as cells respond to the drug; Supplementary Fig. 1c). We considered the 'area of ambiguity' for population growth to be constrained by two assumptions: (1) the population size (for example, live and dead cells) is never less than observed in the initial measurement (y_0) and (2) the population size is never greater than observed in the final measurement (y_{48}). Assumptions 1 and 2 are met if dead cells can be measured using SYTOX (that is, dead cells do not decay to the point that they are no longer SYTOX positive) and live cells can be observed by STYOX following Triton permeabilization. These assumptions were met in our data due to the relatively short duration of our study (48 h) and the durability of SYTOX fluorescence, which we and others find to be stable for at least 72 h[21]. For simplicity we used an exponential population growth model, which assumes a uniform rate of growth over time (Supplementary Fig. 1d). In the context of drug treatment, the growth rate is generally decreased, and this is observable in the cell data before and after permeabilization with Triton cell data, which are constrained by the experimentally observed minimum and maximum total cell numbers at the beginning and end of the assay. From the growth curve, the total number of cells could be determined for each condition at any time between 0 and 48 h. Together with dead cell counts, LF was determined for each drug at all time points and doses measured. Kinetic LFs were modeled using a lag exponential death equation described previously[21]:

$$\mathrm{LF}(t) = \mathrm{LF}_0 + \left(\mathrm{LF}_\mathrm{P} - \mathrm{LF}_0\right) \times \left(1 - e^{-D_\mathrm{R}(t-D_\mathrm{O})}\right)$$

where LF_0 is the lethal fraction at time 0, LF_p is the death plateau, D_O is the onset time of death, and D_R is the maximum rate of death. The model was constrained by $0 < D_\mathrm{O} < 48$, $\mathrm{LF}_\mathrm{p} < 1$ and $D_\mathrm{R} < 2$. LF_0 was left unconstrained to allow for variation in basal levels of cell death. Drugs that did not produce LF_{max} values two times greater than the LF_{max} value for DMSO-treated samples were fit to a linear model.

Notably, this approach makes an assumption about uniform exponential growth for drug-treated cells; however, assay accuracy does not depend on the uniform growth rate assumption. We also tested in 24 population growth models, including many that were not exponential and many with non-uniform growth rates over time, to determine a possible range for LF kinetics (Supplementary Fig. 1d). In general, death kinetic terms (D_O and D_R) were invariant regardless of the population growth model chosen for non-lethal drugs and death-inducing drugs at low and high concentrations. Some variation was observed at intermediate doses for death-inducing drugs, and variation was largest for drugs with particularly early death onset times, as fluctuations in the growth model alter death rates and death plateau values. These data are reported as confidence intervals for death kinetic parameters in Supplementary Dataset 1.

U2OS mKate2 and *BAX*/*BAK* double-knockout cell line generation. NucLight red mKate2 U2OS cells were generated by spinfecting 6.33×10^6 transduction units (TU) per mL of NucLight Red virus (Essen Biosciences) with 8 µg ml^{-1} polybrene and 1.5×10^6 cells at 2,000 r.p.m. for 2 h at 37 °C. After spinning, fresh DMEM was added and the cells were incubated overnight. On the next day, cells were replated onto a 10-cm dish and grown to 80% confluence. mKate2 cells were selected by FACS. The *BAX*/*BAK* DKO U2OS cell line was generated using the pX330-puro plasmid with an hSpCas9 and *BAX* (GACAGGGGCCCTTTTGCTTC) or *BAK* (AGACCTGAAAAATGGCTTCG) sgRNA insert. U2OS cells were transiently transfected using FuGENE HD transfection reagent (Promega). *BAX*/*BAK* DKO cells were selected with BH3-mimetic Navitoclax (10 µM) for 5 d. Following Navitoclax treatment, cells were seeded as single-cell clones and *BAX*/*BAK* DKO cells were confirmed by sequencing.

Quantitative microscopy and STACK image analysis. mKate2-expressing U2OS cells were seeded either at 200,000 cells per well of 6-well plates or at 2,500 cells per well of 96-well plates and adhered overnight. On day 0, drugs were added to wells in addition to 50 nM SYTOX. Images were captured using an EVOS FL Auto microscope with a ×10 objective using GFP (470/510) and Texas Red (585/624) light cubes (Life Technologies). Twenty-five images were collected per well for experiments on 6-well plates and four images per well were collected for experiments on 96-well plates, with two wells per treatment condition. Live-cell and dead-cell counting was performed using IncuCyte software. The average number of cells per image was 284 (range, 108–812). LF was computed as in Forcina et al[21].

Classification of drug mechanisms of cell death. Drugs were classified as non-lethal, apoptotic and non-apoptotic. Non-lethal compounds were those that did not induce significant cell killing over background even at the highest doses tested. Significant killing was defined in this study based on the LF_{max} observed at the assay endpoint. More specifically, the LF values for DMSO treatment reached ~8% at the end of the assay, so drugs were categorized as non-lethal if they induced less than 16% death at their maximum concentration at 48 h. In our kinetic evaluation, these drugs fit to a linear model rather than a lag exponential death model, consistent with the lack of any observable drug-induced increase in the rate of cell killing. For the remaining 45 drugs, apoptotic and non-apoptotic classes were distinguished using a two-pronged approach, with either quantitative thresholds or a multivariate analysis of our pharmacological and kinetic data. Both approaches focused on differences in the measured death between WT and *BAX*/*BAK* DKO cells. For the threshold-based strategy, we characterized apoptotic drugs as those in which the LF_{max} observed in our data in DKO cells was decreased by greater than 50% relative to WT cells (that is, where the death was mostly apoptotic).

To validate these classifications, and to validate the use of a 50% threshold (essentially to avoid the use of any thresholds), we also analyzed the full complement of pharmacological and kinetic data for each drug with PCA. PC1 captured response features related to potency (E_{max}, LF_{max}, etc.), whereas PC2 captured the degree to which responses were changed in DKO versus WT cells (that is, DKO/WT ratio; Supplementary Fig. 3f). Drug classifications based on a 50% difference in DKO versus WT LF_{max} were consistent with PCA projections and also with other data dimensionality reduction methods, such as *t*-SNE. Of note, both PCA- and *t*-SNE-based analyses identified two different groups within the apoptotic class. For 17 drugs, responses were completely lost in DKO cells (that is, both kinetic and dose–response curves fit to a linear model). For the remaining 17 apoptotic drugs, measures of drug response were diminished in DKO cells, although not as dramatically (Supplementary Fig. 3e; two groups of apoptotic drugs with respect to death onset times in DKO cells). In our analyses, these classes were combined into one apoptotic class for simplicity. See also Supplementary Dataset 1.

Drug combination screen. For combinations of cell death-inducing drugs, we used a 'fixed dose ratio' scheme rather than an 'all-by-all' dose matrix (that is, isobologram analysis). For most drugs, the highest drug concentration tested was 31.6 µM; however, to maintain similar levels of potency in the combination drug screen, several drugs were tested starting at higher or lower ranges (Supplementary Dataset 2 and Supplementary Table 3). For graphing purposes, these drugs are plotted on a shared 'normalized' dose axis, reporting two dose scales when needed (Fig. 2e,f). Drug dilutions were pinned onto 96-well plates manually by the following procedure: a source plate contained stock concentrations of 54 drugs arrayed in wells 1–54. From the source plate, each single row of ten drugs was diluted to five times the highest concentration needed in the screen in DMEM using a 12-channel pipette. This array of 54 drugs was considered the 'B drug'. To the array of B drugs, the 'A drug' was added manually at five times highest concentration needed in the screen using a repeat pipettor. For wells in which the A and B drugs were identical (that is, A + A combinations), an equivalent volume of DMSO was added in place of the A drug. Thus, no self–self drug pairs were

tested in this screen, both to conserve drug and to create day-to-day replicates of each drug to evaluate data robustness. These A + B drug combinations in the pin plate were subsequently diluted at half-log dilutions for a total of seven doses. Then, 10 µl of each fivefold drug dilution was added to 384-well plates using an Integra via-flo 96-well head automatic pipettor.

Calculating drug–drug interactions. Drug–drug interactions were calculated using the Chou–Talalay method (CI) and the DBI. The response data used were 1 − LF (that is, with the LF measurement represented in terms of the viable fraction). CI was calculated according to the convention:

$$\mathrm{CI} = \frac{D_A}{d_A} + \frac{D_B}{d_B}$$

where d_a and d_b are the IC_{50} doses of drug A (alone) and drug B (alone), and D_A and D_B refer to the doses of drugs A and B in the A + B combination that resulted in an IC_{50} response. A similar calculation was performed using the EC_{50} of A, B and the A + B combination, as well as the GR_{50} (dose of 50% growth reduction). For the GR index, the relative viability (live cells in drug-treated versus vehicle-treated conditions) was used rather than 1 – LF based on the established convention for the GR index[50]. In figures where a dose curve is shown for a predicted additive drug response, the curve was estimated using three-parameter logistic regression, with the EC_{50} set to the predicted IC_{50} at CI = 1, E_{max} set to the minimum observed between drugs A and B, and the hill slope set to the mean of hill slopes for drugs A and B.

For DBI, the expected response at each dose was computed according to the BI convention:

$$\text{Bliss expected response} = R_A + R_B - (R_A \times R_B)$$

where R_A and R_B refer to the LF observed at each dose for drugs A and B. The Bliss expected response at each dose was then fit to a logistic regression model. DBI was computed as:

$$\mathrm{DBI} = \frac{(\text{AOC Bliss expected response})}{(\text{AOC observed response})}$$

where the AOC was computed for the observed data and the Bliss expected dose–response curve. For each of the methods described above, thresholds for non-additive interactions were determined by comparing the error among biological replicates. Specifically, CI or DBI scores were computed from each replicate separately. Replicate 1 was selected as 'true' and the threshold for drug-drug interaction was iteratively increased from 1 to 10 (for antagonism) or decreased from 1 to 0 (for synergy). This process was repeated using every other replicate as true and evaluating 'hit' specificity using replicate 1. Threshold values for interaction were selected at values where false-positive rates were below 5%. Thresholds and numbers of positive/negative interactions are shown in Supplementary Table 1 and Supplementary Fig. 7.

Quantitative identification of drug combinations featuring single-agent dominance. To identify drug combinations that feature SAD in a quantitative and unbiased manner, we quantified the Euclidean distance between the pharmacological dose curves for every drug combination and its component drugs. A drug was considered dominant if the distance between a drug combination and its closest single drug was less than two times the error rate observed in our assay (that is, less than ~12% variation). This process also selects relatively trivial versions of dominance where the suppressed drug was inefficacious. Thus, we also did not allow suppressed drugs to result in less than 16% killing (the same threshold used to define non-lethal compounds). Using this approach, dominant antagonism was observed for 130 combinations when CI was used to define antagonism and 159 combinations when DBI was used to define antagonism. See also Supplementary Datasets 3 and 4.

CellTiter-Glo-based measurement of relative viability. Cells were seeded at 2,500 cells per well in 96-well plates and adhered overnight. On the day of drug addition, 10× drug solutions were prepared as above in DMEM and added to the wells. At 48 h after treatment, cells were lysed according to the manufacturer's instructions (CellTiter-Glo, Promega) and luminescence was measured using a Tecan Spark I plate reader. Relative viability was calculated as the percentage viability relative to DMSO control wells on the same plate.

Flow cytometry-based analysis of apoptosis. Cells were seeded at 200,000 cells per well in six-well dishes on the day before treatment and adhered overnight. For time-course experiments, drugs were added in a manner such that all samples were collected at the same time. After treatment, cells were collected and fixed with 4% formaldehyde for 15 min. After two washes with PBS, cells were exposed to 100% methanol at −20 °C for > 2 h. Cells were washed with PBS and incubated with antibody to active caspase-3 (1:500 dilution, BD Biosciences) in a 50/50 (vol/vol) PBS-T:Odyssey blocking buffer solution (LICOR). Cells were washed with PBS-T and incubated with Alexa Fluor 647-conjugated primary antibody to cleaved PARP and Alexa Fluor 488-conjugated goat anti-rabbit secondary antibody (1:500 dilution; BD Bioscience) overnight at room temperature. FACS samples were run on an LSR II machine with excitation lasers of 488 and 640 nm.

Western blot analysis of PARylation. Cells were seeded at 200,000 cells per well in six-well dishes and adhered overnight. All drugs were added at $t = 0$, and cell lysates were prepared at indicated time points. Briefly, medium was removed from the well and cells were washed twice with 2 ml of PBS. Cells were lysed by adding 400 µl of SDS-lysis buffer (50 mM Tris-HCl, 2% SDS, 5% glycerol, 5 mM EDTA, 1 mM NaF, 10 mM β-glycerophosphate, 1 mM PMSF, 1 mM Na_3VO_4, protease inhibitor and phosphatase inhibitor tablet). Lysates were spin-filtered through 0.2-µm multi-well filters to remove DNA (Pall). After filtration, lysate concentration was determined by the Pierce BCA protein assay kit according to the manufacturer's instructions (Thermo). Lysate concentrations were normalized to 0.5 mg ml^{-1} for SDS–PAGE loading. Samples were run on precast 48-well gels and transferred using a semidry fast transfer (i-BLOT, Invitrogen). Membranes were blocked in a 50/50 (vol/vol) PBS-T:Odyssey blocking buffer solution for 1 h at room temperature, incubated overnight at 4 °C in primary antibody and stained with secondary antibodies conjugated to infrared dyes (LICOR). Blots were visualized using a LICOR Odyssey CLx scanner.

Data analysis and statistics. All statistical analyses and curve fitting was performed using MATLAB software. PCA was performed after *z*-scoring data using the built-in function 'pca'. Analysis of flow cytometry data was performed using FlowJo, and western blot analysis was done using LICOR Image Studio. Pearson correlation coefficients were calculated using the MATLAB function 'corrcoef'. Fisher's exact tests were performed using the function 'fishertest', with right tailed specified (for example, enrichment). *t*-SNE was performed on *z*-scored data using the function 'tsne' under default conditions.

Reporting Summary. Further information on research design is available in the Nature Research Reporting Summary linked to this article.

Data availability

Source data for evaluation of the mechanism by which drugs led to cell death are included in Supplementary Dataset 1. Source data for the drug combination screen in Fig. 2d are included in Supplementary Dataset th2. PCA score data related to Fig. 4a–c are included in Supplementary Dataset 3. The list of 130 SAD combinations identified in this study is included in Supplementary Dataset 4. All other data are available upon request.

Code availability

Custom analysis code for computing LF kinetics from endpoint data is included in the MATLAB script 'backfitting and LED.m'. Other analysis code is available upon request.

References

50. Hafner, M., Niepel, M., Chung, M. & Sorger, P. K. Growth rate inhibition metrics correct for confounders in measuring sensitivity to cancer drugs. *Nat. Methods* **13**, 1–11 (2016).

Acknowledgements

We thank current and past members of the Lee labotatory and all members of PSB for their helpful comments and critiques during the execution of this study. In addition, we thank M. Walhout, J. Dekker, A. Mitchell and J. Pritchard for their thoughtful comments during the preparation of this manuscript. The px330-puro-hSpCas9 plasmid was a kind gift from T. Fazzio (UMass Medical School). This work was supported by the National Institute of General Medical Sciences of the National Institutes of Health (R01GM127559 to M.J.L.); the American Cancer Society (RSG-17-011-01 to M.J.L.); and an NIH/NCI training grant (Translational Cancer Biology Training Grant, T32-CA130807 to R.R., B.D.L. and P.C.G.).

Author contributions

This project was conceived by R.R. and M.J.L. Combinatorial drug screening was designed, executed and analyzed by R.R., B.D.L. and P.C.G., and M.J.L. helped with the execution of the combination drug screen. Imaging experiments and STACK analysis were performed by R.R. and H.R.S. Drug evaluation and annotation of the drug mechanism of action were performed by R.R., A.J.J., P.C.G. and M.S.S. Flow cytometry-based analyses were performed and analyzed by R.R. and M.E.H. All other statistical analysis and modeling were conducted by R.R., M.E.H. and M.J.L. R.R. and M.J.L. wrote and edited the manuscript.

Competing interests

The authors declare no competing interests.

Additional information

Supplementary information is available for this paper at https://doi.org/10.1038/s41589-020-0510-4.

Correspondence and requests for materials should be addressed to M.J.L.

nature research

Corresponding author(s): Michael J. Lee

Last updated by author(s): Feb 14, 2020

Reporting Summary

Nature Research wishes to improve the reproducibility of the work that we publish. This form provides structure for consistency and transparency in reporting. For further information on Nature Research policies, see Authors & Referees and the Editorial Policy Checklist.

Statistics

For all statistical analyses, confirm that the following items are present in the figure legend, table legend, main text, or Methods section.

n/a	Confirmed	
☐	☒	The exact sample size (*n*) for each experimental group/condition, given as a discrete number and unit of measurement
☐	☒	A statement on whether measurements were taken from distinct samples or whether the same sample was measured repeatedly
☐	☒	The statistical test(s) used AND whether they are one- or two-sided *Only common tests should be described solely by name; describe more complex techniques in the Methods section.*
☒	☐	A description of all covariates tested
☐	☒	A description of any assumptions or corrections, such as tests of normality and adjustment for multiple comparisons
☐	☒	A full description of the statistical parameters including central tendency (e.g. means) or other basic estimates (e.g. regression coefficient) AND variation (e.g. standard deviation) or associated estimates of uncertainty (e.g. confidence intervals)
☐	☒	For null hypothesis testing, the test statistic (e.g. *F*, *t*, *r*) with confidence intervals, effect sizes, degrees of freedom and *P* value noted *Give P values as exact values whenever suitable.*
☒	☐	For Bayesian analysis, information on the choice of priors and Markov chain Monte Carlo settings
☒	☐	For hierarchical and complex designs, identification of the appropriate level for tests and full reporting of outcomes
☒	☐	Estimates of effect sizes (e.g. Cohen's *d*, Pearson's *r*), indicating how they were calculated

Our web collection on statistics for biologists contains articles on many of the points above.

Software and code

Policy information about availability of computer code

Data collection	Data were collected for this study using a Tecan Ml000 plate reader running iControl software version 3.9.1.0; Incucyte microscope using the built-in software version 2019B, LSR II flow cytometer running FacsDiva version 8.0.2 (build 2016 11 22 10 42); LiCOR Odyssey Clx infrared scanner running Image Studio version 3.1.4
Data analysis	All statistical analyses and curve fitting was performed using MATLAB software versions 2017b through 2019b (regular 6 month updated versions). Cell death kinetic estimates were calculated using custom code ('backfitting and LED.m') which is available with the manuscript. PCA was performed in MATLAB after z-scoring data using the built-in function 'pca'. Analysis of flow cytometry data was performed using FlowJo version 10.5.3, and Western blot analysis was done using LICOR Image Studio version 3.1.4. Image analysis was performed either using Incucyte built-in software version 2019B, or custom segmentation code written in MATLAB using the built-in function 'edge'. Pearson correlation coefficients were calculated in MATLAB using the built-in function 'corrcoef. Fisher's exact tests were performed in MATLAB using the built-in function 'fishertest', with right tailed (e.g. enrichment) specified. t-SNE was performed on zscored data in MATLAB using the built-in function 'tsne' under default conditions.

For manuscripts utilizing custom algorithms or software that are central to the research but not yet described in published literature, software must be made available to editors/reviewers. We strongly encourage code deposition in a community repository (e.g. GitHub). See the Nature Research guidelines for submitting code & software for further information.

Data

Policy information about availability of data

All manuscripts must include a data availability statement. This statement should provide the following information, where applicable:

- Accession codes, unique identifiers, or web links for publicly available datasets
- A list of figures that have associated raw data
- A description of any restrictions on data availability

Source data for the evaluation of drug mechanism of cell death are included in Supplementary Dataset 1. Source data for the drug combination screen in Fig. 3d are

included in Supplementary Dataset 2. PCA scores data related to Fig. 5 are included in Supplementary Dataset 3. Source data for SAD combinations are included in Supplementary Dataset 4-5. All other data will be made available upon request.

Field-specific reporting

Please select the one below that is the best fit for your research. If you are not sure, read the appropriate sections before making your selection.

☒ Life sciences ☐ Behavioural & social sciences ☐ Ecological, evolutionary & environmental sciences

For a reference copy of the document with all sections, see nature.com/documents/nr-reporting-summary-flat.pdf

Life sciences study design

All studies must disclose on these points even when the disclosure is negative.

Sample size	Sample sizes for experiments were generally n = 4. These sample sizes were sufficient because effect sizes that are generally considered "non-additive" (combination indices >1.2 or less than 0.8; i.e. 20% difference from expectation) could be recovered with less than 5% false positivity with this sample size. False positive rate was determined by using one set of replicates as a reference standard and determining the reproducibility of these data using the other set of replicates. The overall error rate in our assay was ~ 6%.
Data exclusions	no data were excluded
Replication	Replication of the effects seen in our drug screen was attempted using other common cell death assays. In These data are shown in Supplemental Figure 6. In general, the phenotypes from the screen were replicated at greater than 95% frequency (i.e. > 95% of non-additive interactions from our screen were found to be non-additive upon re-testing). Rate estimates in Figure 2 were repeated on independent days as reported and no data were omitted. The Loewe checkerboard study in Figure 4 was performed on 3 separate days. Following the first attempt the dose range was optimized and these data were not included. Data from the final 2 attempts are included in the figure. The time-staggered MNNG+CAM experiment in Figure 5 was performed on 3 separate days. Following the first attempt the dose range was optimized and these data were not included. Data from the final 2 attempts are included in the figure. The MNNG+CAM crosstalk experiments in Figure 6 were tested as independent biological replicates, but not replicated otherwise.
Randomization	Drugs were not randomized in multi-well plates. To control for plating bias extensive controls were tested to determine the effect of location bias, which for lethal fraction was found to be negligible.
Blinding	Blinding was generally not performed for this study, as the investigators had no prior assumptions/bias regarding expected outcomes (e.g. the data and analysis are the result of a large "screening" study).

Reporting for specific materials, systems and methods

We require information from authors about some types of materials, experimental systems and methods used in many studies. Here, indicate whether each material, system or method listed is relevant to your study. If you are not sure if a list item applies to your research, read the appropriate section before selecting a response.

Materials & experimental systems

n/a	Involved in the study
☐	☒ Antibodies
☐	☒ Eukaryotic cell lines
☒	☐ Palaeontology
☒	☐ Animals and other organisms
☒	☐ Human research participants
☒	☐ Clinical data

Methods

n/a	Involved in the study
☒	☐ ChIP-seq
☐	☒ Flow cytometry
☒	☐ MRI-based neuroimaging

Antibodies

Antibodies used

Poly/Mono ADP Ribose Rabbit mAb (Cell Signaling Technolgies; Catalog number 83732; Clone E6F6A; Lot #1; 1:1000 dilution)
Purified rabbit anti-active caspase 3 (BD Pharmingen; Catalog number 559565; Clone [unknown]; Lot #8256780; 1:500 dilution)
Alexa Fluor® 647 conjugated mouse anti-cleaved PARP (BD Pharmingen; Catalog number 558710; Clone F21-852; Lot #5253919; 1:250 dilution)
beta-actin mouse (Sigma; Catalog number A5441; Clone AC-15; Lot# [unknown]; 1:15,000 dilution)
Li-COR Goat anti-rabbit secondary 800CW (Li-COR Biosciences; Catalog number 926-32211; Clone [unknown]; Lot #C30626-03; 1:15,000 dilution
Li-COR Goat anti-mouse secondary 680RD (Li-COR Biosciences; Catalog number 926-68070; Clone [unknown]; Lot #C30723-04; 1:15,000 dilution
Alexa Fluor488 Goat anti-rabbit secondary IgG(H+L) (Invitrogen; Catalog number A11008; Clone [unknown]; Lot #1937184; 1:250 dilution

Validation	For these commercial antibodies, appropriate dilutions and staining conditions were determined using positive and negative controls, which were drugs that induced cell death using known death subtypes (doxorubicin for apoptotic signals; MNNG for parthanatotic signals).

Eukaryotic cell lines

Policy information about cell lines

Cell line source(s)	U2OS, MDA-MB-231, A549, MCFl0A were all obtained from ATCC
Authentication	cell lines were authenticated using STR profiling
Mycoplasma contamination	Cell lines were tested for mycoplasma contamination annually and only cells confirmed as mycoplasma negative were used in this study.
Commonly misidentified lines (See ICLAC register)	no commonly misidentified lines were used in this study

Flow Cytometry

Plots

Confirm that:

☒ The axis labels state the marker and fluorochrome used (e.g. CD4-FITC).

☒ The axis scales are clearly visible. Include numbers along axes only for bottom left plot of group (a 'group' is an analysis of identical markers).

☒ All plots are contour plots with outliers or pseudocolor plots.

☒ A numerical value for number of cells or percentage (with statistics) is provided.

Methodology

Sample preparation	Post treatment, cells were collected and fixed with 4% formaldehyde for 15 minutes. After two washes with PBS, cells were exposed to 100% methanol at -20oC for >2 hours. Cells were washed with PBS and incubated with the active caspase-3 antibody (1:500 dilution, BD Biosciences) in a 50/50 (v/v) PBS-T:Odyssey blocking buffer solution (LICOR). Cells were washed with PBS-T and incubated with the Alexa-fluor 647 cleaved PARP primary and Alexa-fluor 488 goat anti-rabbit secondary antibodies (1:250 dilution, BD Bioscience) overnight at room temperature.
Instrument	FACS samples were run on an LSR II machine with excitation lasers of 488 and 640 nm.
Software	Data were analyzed using FlowJo version 10.0
Cell population abundance	Data are from 10,000 gated cells.
Gating strategy	A simple gating strategy was used in which a FSC/SSC was used to identify a single population of cells, removing cellular debris.

☒ Tick this box to confirm that a figure exemplifying the gating strategy is provided in the Supplementary Information.